

Bayes2IMC: In-Memory Computing for Bayesian Binary Neural Networks

Prabodh Katti, *Student Member, IEEE*, Clement Ruah, *Student Member, IEEE*, Osvaldo Simeone, *Fellow, IEEE*, Bashir M. Al-Hashimi, *Fellow, IEEE*, Bipin Rajendran, *Senior Member, IEEE*,

Abstract—Bayesian Neural Networks (BNNs) provide superior estimates of uncertainty by generating an ensemble of predictive distributions. However, inference via ensembling is resource-intensive, requiring additional entropy sources to generate stochasticity which increases resource consumption. In this work, we introduce Bayes2IMC, an in-memory computing (IMC) architecture designed for binary Bayesian neural networks that leverage nanoscale device stochasticity to generate desired distributions. Our novel approach utilizes Phase-Change Memory (PCM) to harness inherent noise characteristics, enabling the creation of a binary neural network. This design eliminates the necessity for a pre-neuron Analog-to-Digital Converter (ADC), significantly improving power and area efficiency. We also develop a hardware-software co-optimized correction method applied solely on the logits in the final layer to reduce device-induced accuracy variations across deployments on hardware. Additionally, we devise a simple compensation technique that ensures no drop in classification accuracy despite conductance drift of PCM. We validate the effectiveness of our approach on the CIFAR-10 dataset with a VGGBinaryConnect model containing 14 million parameters, achieving accuracy metrics comparable to ideal software implementations as well as results reported in the literature using other technologies. Finally, we present a complete core architecture and compare its projected power, performance, and area efficiency against an equivalent SRAM baseline, showing a 3.8 to $9.6\times$ improvement in total efficiency (in GOPS/W/mm²) and a 2.2 to $5.6\times$ improvement in power efficiency (in GOPS/W). In addition, the projected hardware performance of Bayes2IMC surpasses that of most of the BNN architectures based on memristive devices reported in the literature, and achieves up to 20% higher power efficiency compared to the state-of-the-art.

Index Terms—Bayesian Neural Networks, PCM, In-Memory Computing.

I. INTRODUCTION

A. Context and Motivation

THE growing demand for edge AI in applications such as medical diagnostics [1], facial identification and surveillance [2] and self-driving cars [3] where reliability and safety are of paramount importance, has heightened the need for systems that provide a measure of uncertainty while operating under significant resource constraints in terms of area and power. Advances in deep neural networks have ensured very high accuracy, but this has come at the cost of overconfidence and poor calibration [4]. More importantly, such networks are incapable of uncertainty quantification, especially out-of-distribution identification measured by epistemic uncertainty.

[5]. Bayesian neural networks (BNNs) overcome this problem by allowing the weight parameters to be probability distributions rather than point estimates, thus encoding uncertainty in the parameter distributions [6], [7]. During inference, the network weights are then sampled to create an ensemble, and the outputs are combined in Monte-Carlo (MC) fashion to obtain predictions, confidence and uncertainty (Fig. 1). The creation of ensembles can be done in time, i.e., instantiating each ensemble one after another on the same hardware [8], or in space, i.e., instantiating all the ensembles simultaneously, using multiple copies of the hardware [6]. Both methods are resource-intensive compared to a traditional network whose parameters are point estimates and require only a single instantiation. The ensembling-in-time approach reduces net decision-making throughput while optimizing for power and total area. In contrast, the ensembling-in-space expends more area and power in order to deliver high net throughput. In addition, both these approaches require noise sources to generate random numbers. Thus, the deployment of Bayesian neural networks at the edge is challenging and requires careful hardware-software co-optimization [9], [10].

In this paper, we design and validate an area and power-efficient ensembling-in-time Bayesian binary neural network in-memory compute (IMC) architecture named Bayes2IMC that leverages the inherent stochasticity of nanoscale memory devices. Fig. 1 provides a high-level description of this core. The nanoscale devices are arranged in a crossbar fashion, which is partitioned into two sections: a weight plane (WP) that stores the distribution parameters, and a noise plane (NP) that provides stochasticity necessary for sampling [6]. We also modify the traditional in-memory computing approach by routing inputs to an accumulator for multiply-and-accumulate (MAC) operations. This combination of routing strategy, row-by-row read flow, and on-the-fly sample generation during sensing enables inference without the need for an analog-to-digital converter, thereby improving area and power efficiency.

B. Background and Related Work

In-Memory Computing: The IMC approach has been proposed to address the ‘von Neumann bottleneck’ [11] plaguing traditional computing platforms [12]–[16]. In such systems, certain computational operations are performed in memory without data movement, enabling high throughput at low area and power. IMC implementations based on digital Static Random Access Memories (SRAMs) [16]–[20] as well as those based on non-volatile memory (NVM) devices such as Phase Change Memory (PCMs), Resistive RAMs (RRAMs), Spin-Transfer Torque RAMs (STT-RAMs), and Spin-Orbit Torque Magnetic

The authors are affiliated with the Centre for Intelligent Information Processing Systems (CIIPS), Department of Engineering, King’s College London, London WC2R 2LS, U.K. (bipin.rajendran@kcl.ac.uk)

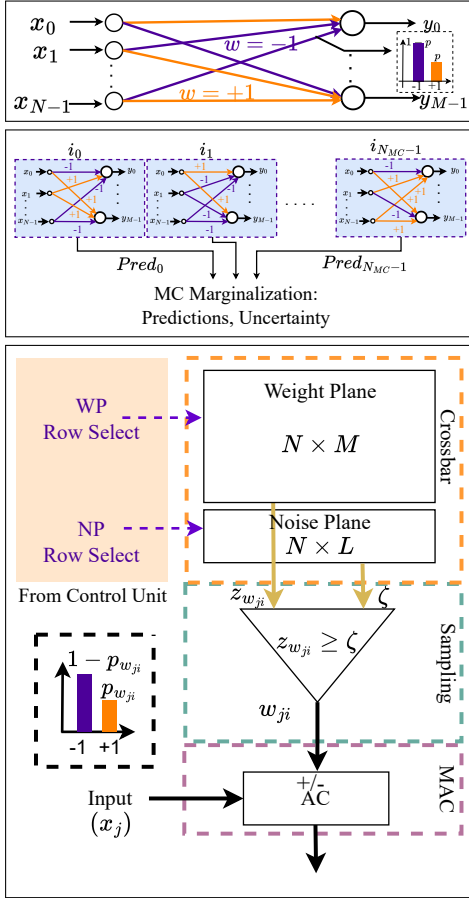


Fig. 1: **Top:** Illustration of a Bayesian neural network (BNN) where weights take binary values upon sampling. **Middle:** Bayesian inference is performed by an ensemble of N_{MC} predictions combined through Monte Carlo sampling to obtain predicted class, prediction confidence, and uncertainty. **Bottom:** Block diagram of the proposed Bayes2IMC core architecture implementing BNN inference. The crossbar array of memristive devices is divided into a weight plane (WP) and a noise plane (NP). The WP stores the parameters $z_{w_{ji}}$ obtained by reparametrizing the probability parameters $p_{w_{ji}}$, and the noise plane generates the stochasticity required for synaptic sampling. Binary weights w_{ji} are then generated by comparing these variables in hardware. Unlike traditional IMC architectures, the input x_j , j^{th} element of input vector \mathbf{x} , is accumulated based on the sign of w_{ji} .

RAMs (SOT-MRAMs) have been explored for implementing frequentist deep learning models [14], [21], [22]. Compared to SRAM IMC implementations, NVM devices have following advantages:

- Multi-level conductance for multi-bit parameter storage.
- Near $\mathcal{O}(1)$ matrix-vector multiplication (MVM) operation when arranged in crossbar fashion with input vector encoded as drive voltage [23].

However, NVM devices also pose several challenges for IMC MVM implementation. The high level of state-dependent programming [24] results in write error, and conductance drift results in instability of programmed weights [10], [24]. This severely impacts the overall classification accuracy. Additional

sources of error include MVM errors due to IR drops on source-line due to high current in the all-parallel operation mode [18], and non-linear dependence of device current on applied voltage [25]. Furthermore, Analog-to-Digital converters (ADCs) are necessary to convert the analog output of the MVM operation to multi-bit digital values, and this impacts both the overall power consumption and area efficiency [12], [18].

Related works: We now discuss proposed IMC solutions in the literature that leverage the inherent stochasticity of NVM devices with the goal of implementing ensembling methods. An RRAM array-based Bayesian network with training implemented via Markov Chain Monte Carlo (MCMC) was demonstrated in [26], though the need for training in situ is time and resource intensive [27]. Bernoulli distributed noise of Domain Wall Magnetic Tunnel Junction (DW-MTJ) devices and SOT-MRAM were used in [21] and [9] respectively to generate Gaussian random variables. The latter uses a local reparametrization technique to reduce resource consumption. However, both of these works require the mean and standard deviation parameters to be stored separately and the contributions from multiple devices to be combined to generate a single random variate per the central limit theorem. This lead to expensive hardware requirements.

An efficient implementation was presented in [10] that performs device-aware training and combines multiple devices to generate the required stochasticity per weight parameter. The authors of [28] use STT-RAM to implement binary neural networks and perform Bayesian inference using Monte-Carlo Dropout (MCD) methods [29], where neurons are randomly dropped out during inference leveraging a random number generated using STT-RAM's stochasticity. While MCD-based networks are easy to train and deploy, they are reported to be less expressive, especially for out-of-distribution uncertainty estimations [30], [31].

To mitigate effects of conductance drift, periodic calibrations of each layer of the network was used to obtain optimal affine factors to reduce error in [24]. Alternatively, [10], proposed reprogramming at different time intervals based on the effect of drift on the available domain of programmable conductance values. However, this involves multiple reprogramming steps, which is resource-intensive.

Many of these works also employ a digital-to-analog-converter (DAC) to provide analog voltage input vectors. This can result in errors due to I-V non-linearity in some devices, as discussed in [25]. Working around this problem, references [9], [10], [18] propose bit-slicing, wherein the input bits are sent one by one, and the accumulated outputs after analog-to-digital conversion are scaled by their binary positional weights and summed. Pulse width modulation (PWM) can also be used, as suggested in [13]. In addition to extra circuitry overhead – shift-and-add circuits in the former or PWM generator in the latter – all the methods described require an ADC for readout, which consumes up to 87% power and 60% of the total area of a core [12], [22]. To reduce the power and area overhead, the ADC use is typically multiplexed amongst several columns, affecting the overall throughput [18].

C. Main Contributions

In this work, we introduce Bayes2IMC, a PCM-based computing architecture designed for BNNs with binary weights. Binary BNNs are less resource-intensive because they need only one parameter to describe the weight distribution. The main contributions of the paper are as follows:

- We formulate a principled way to utilize the inherent device stochasticity as a noise source for ensembling.
- We devise a hardware-software co-optimized technique that is applied only on the output logits to reduce accuracy variations across multiple network deployments.
- We propose a simple global drift compensation mechanism to reverse the effect of state-dependent conductance drift on network performance. This does not require frequent reprogramming or layer-by-layer calibration, only a simple rescaling of the read pulse. Our approach ensures no drop in accuracy, expected calibration error (ECE) [4] and uncertainty performance up to 10^7 seconds.
- By introducing row-by-row read, we avoid high output currents. Additionally, every read operation handles the binarization in tandem without requiring any throughput throttling step. This permits an ADC-less architecture, significantly improving the efficiency of the design.
- We avoid using DACs at every row by streaming inputs directly into pre-neuron accumulator and applying fixed width and amplitude read pulses on bit-lines to sample weights. By doing so, we improve the area and power efficiency and avoid the MVM errors due to the non-linear dependence of device conductance on applied voltages.

To the best of our knowledge, this is the first work to demonstrate variational inference-based binary BNNs on IMC. We achieve a projected total efficiency improvement of 3.8–9.6× as compared to an equivalent SRAM architecture.

The rest of the paper is organized as follows. In Section II, we review background material on Bayesian neural networks, uncertainty quantification and PCM devices. In Section III, we discuss the design, architecture and the co-optimization between algorithm or software and hardware. The accuracy performance and the hardware projections are discussed in Section IV. Finally, Section V concludes the paper.

II. PRELIMINARIES

In this section, we review preliminary material on binary BNNs (BBNN), calibration measures, aleatoric and epistemic uncertainties and PCM devices.

A. Binary Bayesian Neural Networks

Given a parameterized predictor $p(y|\mathbf{x}, \mathbf{w})$ with parameter vector $\mathbf{w} \in \mathcal{W}$, Bayesian learning amounts to the evaluation of the posterior distribution $p(\mathbf{w}|\mathcal{D})$, quantifying the likelihood of each parameter \mathbf{w} under the evidence presented by the training dataset $\mathcal{D} = \{x_i, y_i\}_i$. At inference time, the contribution of each model $p(y|\mathbf{x}, \mathbf{w})$ is weighted by the posterior $p(\mathbf{w}|\mathcal{D})$ [30], [32], yielding the marginal distribution

$$p(y|\mathbf{x}, \mathcal{D}) = \int_{\mathcal{W}} p(y|\mathbf{x}, \mathbf{w})p(\mathbf{w}|\mathcal{D})d\mathbf{w} = \mathbb{E}_{p(\mathbf{w}|\mathcal{D})} [p(y|\mathbf{x}, \mathbf{w})]. \quad (1)$$

In this work, we focus on the implementation of BBNNs, where each weight $w \in \mathbf{w}$ of the neural network $\mathbf{f}_{\mathbf{w}}(\mathbf{x}) = \{p(y|\mathbf{x}, \mathbf{w})\}_y$ is restricted to a binary set of values $w \in \{-1, 1\}$. Accordingly, the parameter space is defined as $\mathcal{W} = \{-1, 1\}^{|\mathbf{w}|}$, where $|\mathbf{w}|$ represents the number of synaptic weights. Intuitively, BBNNs implement a set of neural networks $\{\mathbf{f}_{\mathbf{w}}\}_{\mathbf{w} \sim p(\mathbf{w}|\mathcal{D})}$ where the weights are trained to follow a posterior distribution $p(\mathbf{w}|\mathcal{D})$ rather than a single point-estimate [30]. Bayesian learning for BBNN is performed through mean-field variational inference (VI) [33], [34]. The posterior distribution $p(\mathbf{w}|\mathcal{D})$ is approximated by a parameterized distribution $q(\mathbf{w}|\boldsymbol{\lambda})$, where $\boldsymbol{\lambda}$, the variational parameter, is the vector of natural parameters of Bernoulli distribution λ_w in the exponential family, i.e $\boldsymbol{\lambda} = \{\lambda_w\}_{w \in \mathbf{w}} \in \mathbb{R}^{|\mathbf{w}|}$. The probability parameter p_w describing the distribution of binary weights w is encoded as

$$p_w = \frac{1}{1 + e^{-2\lambda_w}}. \quad (2)$$

$\boldsymbol{\lambda}$ is trained using the evidence lower bound (ELBO) criterion or free energy, which can be represented as [35]

$$\min_{\boldsymbol{\lambda}} \mathbb{E}_{q(\mathbf{w}|\boldsymbol{\lambda})} [\mathcal{L}_D(\mathbf{w})] + \text{KL}(q(\mathbf{w}|\boldsymbol{\lambda})||p(\mathbf{w})), \quad (3)$$

where $\text{KL}(\cdot||\cdot)$ is the KL divergence.

After training, we obtain a collection of synaptic probabilities $\mathbf{p}_{\mathbf{w}} = \{p_w\}_{w \in \mathbf{w}}$ from (2) which, using an appropriate binary random variable generator, can be leveraged to create an ensemble of networks $\mathbf{f}_{\mathbf{w}}$ with $\mathbf{w} \sim q(\mathbf{w}|\boldsymbol{\lambda})$. As illustrated in Fig. 1, during inference, the outputs $p(y|\mathbf{x}, \mathbf{w})$ of the sampled networks $\hat{\mathbf{f}}_{\mathbf{w}}$ are accumulated and processed to obtain the final marginal predictor

$$p(y|\mathbf{x}, \mathcal{D}) = \mathbb{E}_{\mathbf{w} \sim q(\mathbf{w}|\boldsymbol{\lambda})} [p(y|\mathbf{x}, \mathbf{w})] \approx \frac{1}{N_{MC}} \sum_{i=1}^{N_{MC}} p(y|\mathbf{x}, \mathbf{w}_i), \quad (4)$$

where N_{MC} is the number of independent and identically sampled (i.i.d.) networks $\{\mathbf{w}_i\}_{i=1}^{N_{MC}} \stackrel{\text{i.i.d.}}{\sim} q(\mathbf{w}|\boldsymbol{\lambda})$ [30], [34]. We focus on classification tasks in this paper, where the target variable y takes values in a discrete set $\mathcal{C} = \{0, 1, \dots, n-1\}$ for $n \geq 1$. Accordingly, from the set confidence levels $\{p(y|\mathbf{x}, \mathcal{D})\}_{y \in \mathcal{C}}$, a prediction is obtained as $\hat{y} = \text{argmax}_{y \in \mathcal{C}} \{p(y|\mathbf{x}, \mathcal{D})\}$.

B. Expected calibration error (ECE)

The ECE quantifies the in-distribution calibration of a trained network by quantifying the expected discrepancy between accuracy and the confidence scores obtained by the output probability of the predicted class. For a given dataset $\mathcal{D} = \{x_i, y_i\}_{i=1}^{N_s}$ of N_s samples, we denote as $B_m = \{(\hat{p}_i, \hat{y}_i, y_i)\}_{i|\hat{p}_i \in I_m}$ the set of confidence-label pairs for which the predicted confidence $\hat{p}_i = p(y_i|x_i, \mathcal{D})$ lies inside I_m , with $m \in \{1, \dots, N_b\}$. ECE is mathematically described, as per [4], as

$$ECE = \sum_{m=1}^{N_b} \left| \frac{|B_m|}{N_s} \left| \text{acc}(B_m) - \text{conf}(B_m) \right| \right|, \quad (5)$$

where $\text{acc}(B_m) = \frac{1}{|B_m|} \sum_{(\hat{y}, y) \in B_m} \delta_{\{\hat{y}=y\}}$ is the number of correctly predicted samples in B_m and $\text{conf}(B_m) = \frac{1}{|B_m|} \sum_{\hat{p} \in B_m} \hat{p}$ is the average confidence or probability of the predicted class in the interval.

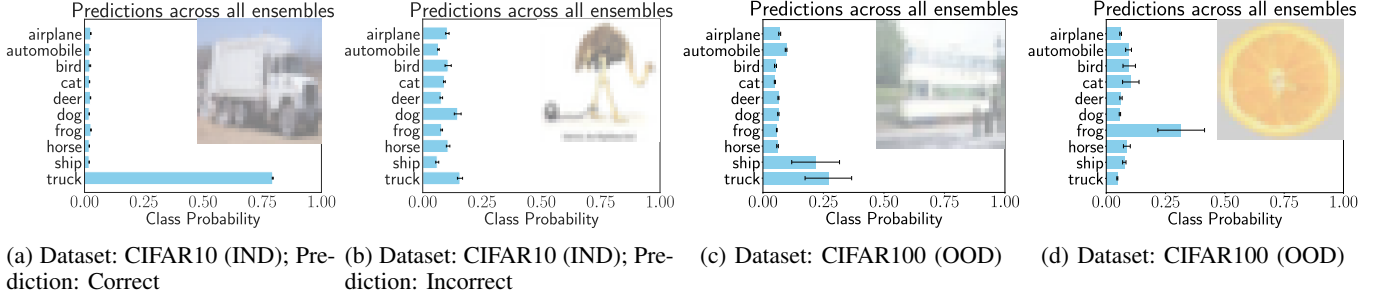


Fig. 2: Illustration of aleatoric and epistemic uncertainty using sample images from the CIFAR10 and CIFAR100 datasets. The results shown are generated from the outputs of a neural network implemented with Bayes2IMC architecture on a custom PCM simulator. This network was trained on the CIFAR10 dataset. Given that CIFAR100 and CIFAR10 contain mutually exclusive classes, the CIFAR100 dataset was utilized to evaluate OOD detection performance. The error bars indicate the variability of probabilities, capturing disagreement amongst predictors in the ensemble.

C. Aleatoric and Epistemic Uncertainty

For a given covariate \mathbf{x} , the total uncertainty of the predictions can be quantified by computing the entropy of the ensemble predictor $p(y|\mathbf{x}, \mathcal{D})$ [10],

$$U_{tot} = \mathbb{E}_{y \sim p(y|\mathbf{x}, \mathcal{D})} [-\log(p(y|\mathbf{x}, \mathcal{D}))] \\ \approx - \sum_{y \in \mathcal{C}} \frac{1}{N_{MC}} \sum_{i=1}^{N_{MC}} p(y|\mathbf{x}, \mathbf{w}_i) \log \left(\frac{1}{N_{MC}} \sum_{i=1}^{N_{MC}} p(y|\mathbf{x}, \mathbf{w}_i) \right), \quad (6)$$

where $\{\mathbf{w}_i\}_{i=1}^{N_{MC}} \stackrel{i.i.d.}{\sim} q(\mathbf{w}|\lambda)$ and $p(y|\mathbf{x}, \mathbf{w}_i)$ is the probability value for the given class $y \in \mathcal{C}$. This total uncertainty U_{tot} can be decomposed into the uncertainty due to the inherently stochastic nature of the covariate-label pairs (\mathbf{x}, y) , i.e., the aleatoric uncertainty; and the uncertainty stemming from the limited amount of evidence \mathcal{D} , i.e., the epistemic uncertainty.

Aleatoric uncertainty can be quantified by the entropy of the labels $y \sim p(y|\mathbf{x}, \mathbf{w})$ with average evaluated with respect to the random parameters $\mathbf{w} \sim q(\mathbf{w}|\lambda)$, which is given mathematically as

$$U_a = \mathbb{E}_{\mathbf{w} \sim q(\mathbf{w}|\lambda), y \sim p(y|\mathbf{x}, \mathbf{w})} [-\log(p(y|\mathbf{x}, \mathbf{w}))] \\ \approx - \frac{1}{N_{MC}} \sum_{y \in \mathcal{C}} \sum_{i=1}^{N_{MC}} p(y|\mathbf{x}, \mathbf{w}_i) \log(p(y|\mathbf{x}, \mathbf{w}_i)), \quad (7)$$

for $\{\mathbf{w}_i\}_{i=1}^{N_{MC}} \stackrel{i.i.d.}{\sim} q(\mathbf{w}|\lambda)$. The epistemic uncertainty is evaluated instead as the difference between the total uncertainty and aleatoric uncertainty, i.e.,

$$U_e = U_{tot} - U_a. \quad (8)$$

Epistemic uncertainty is zero when the mean predictor $p(y|\mathbf{x}, \mathcal{D})$ agrees with each individual predictor $p(y|\mathbf{x}, \mathbf{w})$ of the ensemble, and is positive when they disagree. Note that for frequentist networks with fixed weights, $U_{tot} = U_a$, and therefore $U_e = 0$.

Ideally, for an out-of-distribution (OOD) data, the ensemble of predictors will disagree on predictions, causing a large epistemic uncertainty. In contrast, on In-distribution (IND) data, there should be a broad agreement on the prediction probabilities, and thus the epistemic uncertainty should be low.

Fig. 2 illustrates the distinct roles that aleatoric and epistemic uncertainties play in understanding the predictions of a BBNN. Fig. 2a and Fig. 2b consider the output of the BBNN to IND data. For inputs characterized by a higher confidence in the prediction hence a lower aleatoric uncertainty. The higher aleatoric in the latter case suggests low prediction confidence. In addition, and by a lower prediction confidence hence higher aleatoric uncertainty respectively. In addition, the epistemic uncertainty is low in both cases. This suggests that the incorrect prediction is due to data uncertainty rather than the model's lack of confidence in its predictions. Fig. 2c and Fig. 2d consider OOD data, in which case the high epistemic uncertainties indicate the disagreement amongst the ensembles due to the unfamiliar nature of the inputs.

D. PCM

Phase change memory (PCM) devices consist of chalcogenide materials such as $\text{Ge}_2\text{Sb}_2\text{Te}_5$, sandwiched between two metal electrodes. By adjusting the proportion and arrangement of the crystalline and amorphous phases of the chalcogenide material, PCM devices can be programmed to multiple analog non-volatile conductance states. [36], [37]. Programming a PCM device involves applying electric pulses, wherein the number, amplitude, and duration of these pulses are adjusted iteratively until the desired conductance is attained. The conductance thus programmed exhibits stochasticity that is observed to be state-dependent [38].

To facilitate the implementation of PCM devices in synaptic networks, they can be configured as a differential pair allowing for the storage of both positive and negative weight. Such differential-pair cells arranged in a crossbar fashion enable in-memory computing of matrix-vector multiplication operation [24], [38]. Fig. 3 depicts the noise obtained from measurements of over 10,000 devices in [24]. PCM devices exhibit the following forms of non-idealities:

- Programming noise $\sigma_p(G)$ – also called write noise as it causes deviation from desired conductance upon writing to memory – is attributed to the inherent stochasticity of crystallization process [36]. These variations are approximately Gaussian distributed with a state-dependent standard deviation.
- The read noise $\sigma_r(G)$, due to fluctuations arising from $1/f$ noise [36], [39], is of smaller magnitude as compared

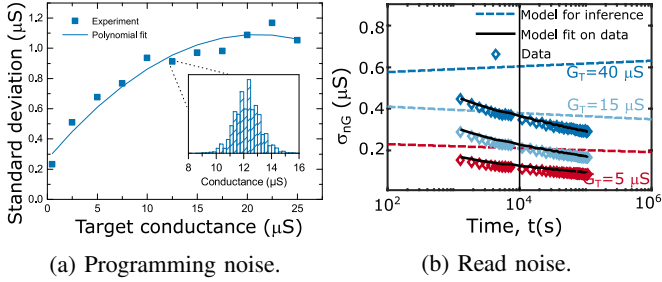


Fig. 3: PCM device noise, taken from [24]. All of these non-idealities are state-dependent.

to the programming noise.

- Conductance drift causes a reduction of PCM conductance over time. This is due to structural relaxation phenomenon affecting primarily the amorphous phase of the material [36], [40], with the drift rate also being a state-dependent parameter [24].

III. ARCHITECTURE AND DESIGN

In this section, we discuss the features of Bayes2IMC, our proposed architecture illustrated in Fig. 1. We first introduce the mathematical techniques that allow the utilization of device stochasticity as a source of noise distribution in Sec. III-A and the corresponding hardware implementation in Sec. III-B. We then describe the details the core operations of the proposed Bayes2IMC architecture (Sec. III-C) and introduce the proposed output logit correction scheme (Sec. III-D). Finally, Sec III-E discusses the drift compensation mechanism.

A. Overview

To generate a sample of the network weight in hardware, we need two key elements:

- 1) Parameters that fully describe the weight distribution. For binary BNNs, this amounts to storing one parameter per weight, the probability parameter p_w of the weight w where, $p_w = \Pr(w = +1)$.
- 2) A noise source that generates a standard distribution, e.g., the uniform distribution $\mathcal{U}(0, 1)$ or the Gaussian distribution $\mathcal{N}(0, 1)$.

The sample weight is then generated by comparing the parameter p_w with a random variable $r \sim \mathcal{U}(0, 1)$ [8], i.e.,

$$w = \begin{cases} +1 & \text{if } r \leq p_w, \\ -1 & \text{if } r > p_w. \end{cases} \quad (9)$$

These sample weights make up the layers of the network mapped across cores, with each core performing the MVM operation

$$y_i^c = \sum_{j=1}^M x_j^c w_{ji}^c, \quad (10)$$

where $\mathbf{x}^c = [x_1^c, \dots, x_M^c]^\top$ is the core input, w_{ji}^c are the binary weights indexed by j and i in the weight matrix and y_i^c is the i^{th} element of output vector \mathbf{y}^c .

The parameters $\mathbf{p}_w = \{p_w\}_{w \in w}$ required for sample generation are stored in WP. The noise, provided by the NP, is due to the inherent device-to-device and cycle-to-cycle

TABLE I: Glossary of variables used in the text

Variable	Definition	Values/Remarks
w	Binary weight	$w \in \{+1, -1\}$
p_w	Probability parameter for w	$p_w \in [0, 1]$
λ_w	Natural parameter for w	$\lambda_w \in (-\infty, \infty)$
z_w	Reparametrized p_w	$z_w \in (-\infty, \infty)$
λ_{clip}	Clipping value for λ_w	± 3.3
z_{clip}	Clipping value for z_w	± 3
f_{σ_p}	Programming noise model	as per Fig. 3a
κ	z_w to G_w scale	8
n_r	No. of NP rows read in parallel	$n_r \in \{1, 2\}$
T_{WP}	WP read pulse width	-
T_{NP}	NP read pulse width	-

stochasticity represented by the state-dependent programming noise shown in Fig. 3. This Weight Plane-Noise Plane (WP-NP) crossbar array architecture introduced in [6], assigns M rows for the weight probability parameters, and L rows in the NP to generate the required stochasticity. We reuse the hardware resource for sampling (i.e., $L \ll M$) and empirically show that this does not affect network accuracy, leading to improved area efficiency. Noise cells from NP and weight cells from WP combine to generate w . We now elaborate the details of this sampling utilizing device stochasticity.

B. Leveraging Device Stochasticity

Reparameterization: To generate network parameters as per (9), we require a source of Uniform noise. However, the naturally available stochasticity from the PCM-based NP in the array is Gaussian distributed. One method to utilize the hardware-provided noise is to soft-binarize the natural parameter described in (2) using the Gumbel-Softmax trick [6], [7], [34], [41]. To make this method amenable to implementation on PCM, the stochastic parameter in the soft-binarization term given in [34] would need to be approximated to a Gaussian random variable (RV) by Gaussian fitting, as described in [6]. We develop a more principled method for sampling binary weights from Gaussian distribution by reparameterizing p_w as

$$z_w = \Phi^{-1}(p_w), \quad (11)$$

where Φ is the cumulative distribution function (CDF) of $\mathcal{N}(0, 1)$ and Φ^{-1} is its inverse. As illustrated in Fig. 4, the each weight w is then independently sampled as

$$w = \begin{cases} +1 & \text{if } \zeta \leq z_w, \\ -1 & \text{if } \zeta > z_w, \end{cases} \quad (12)$$

with $\zeta \sim \mathcal{N}(0, 1)$.

To represent positive and negative parameter values in the crossbar, a differential pair of PCM devices is used. Each differential PCM (DPCM) cell, whether in WP or NP has two devices, programmed to conductances G^+ and G^- . Let the $\sigma_p(G)$ and $\sigma_r(G)$ denote programming and read noise for a given device with conductance G . We denote the conductance of a cell in weight plane storing parameter z_w as G_w , and the conductance of the noise plane cell as G_n .

Noise source: By programming the NP cells such that that $G_n^+ \approx G_n^- \approx G_n$, the mean conductance read out from this cell almost vanishes, while the noise adds up. Programming noise has the dominant effect on the total noise of the noise plane cell as it is significantly larger than read noise as per

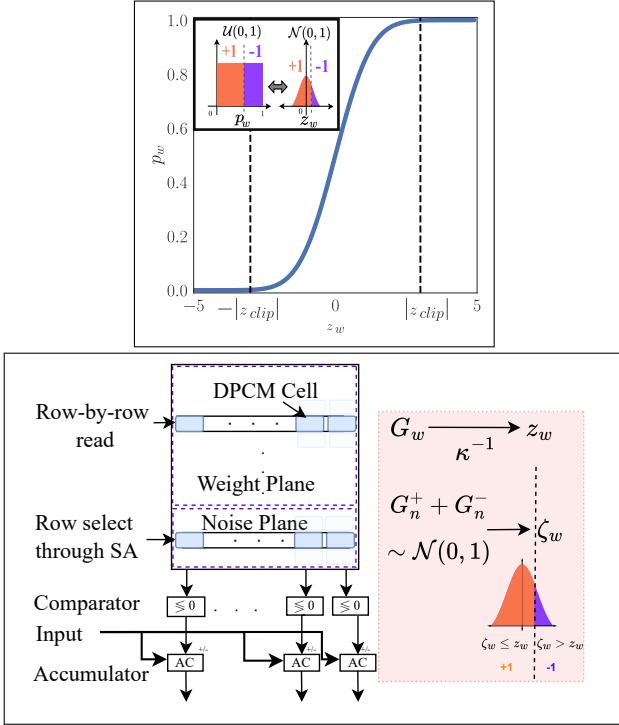


Fig. 4: **Top:** Probability parameter p_w as a function of z_w . z_w is clipped to $|z_{clip}| = 3$. The error in p_w due to these clippings is negligible. *Inset:* Illustration of equivalence of Uniform sampling with p_w and Gaussian sampling with z_w . **Bottom:** Detailed illustration of generating weight samples and MVM operation. Weight plane cells are read row-by-row. Simultaneously, a noise plane row is selected through stochastic arbitration (SA). Read pulse magnitudes of WP and NP are adjusted to restore WP parameters to their original scale. Their currents are summed as per Kirchoff's law and binarized to complete the operation described in (12). The binarized value is used to determine the sign of inputs being accumulated, accomplishing the MAC operation.

Fig. 3. Accordingly, the generated noise parameters are be approximated as

$$\mu_n = G_n^+ - G_n^- \approx 0, \quad (13)$$

$$\sigma_n^2 = \sigma_p^2(G_n^+) + \sigma_p^2(G_n^-) + \sigma_r^2(G_n^+) + \sigma_r^2(G_n^-) \quad (14)$$

$$\approx 2\sigma_p^2(G_n). \quad (15)$$

Our goal is to generate $\zeta \sim \mathcal{N}(0, 1)$ from each noise cell, as per (12). Therefore, G_n must be chosen such that the σ_n as per (15) is equal to 1, and can be identified from the programming noise model f_{σ_p} shown in Fig. 3a.

Mapping parameters to WP: We now discuss the mapping strategy of a WP cell, with weight w and the parameter z_w . We first scale up z_w by a factor κ to get G_w which allows the full use of the available conductance dynamic range of the device. It also reduces the impact of both programming and read noise in WP, ensuring that only the NP noise determines the generation of the weight samples [6].

The dynamic range available to the DPCM cell is $[0, 25 \mu\text{S}]$, which means that the $|z_w|$ has to be clipped to some maximum value (denoted $|z_{clip}|$). For our experiments, we choose $|z_{clip}| = 3$ and map to networks after scaling it by

$\kappa = 8$, ensuring that we can map the entire required range of $0 \leq p_w \leq 1$. Empirically, we observed that λ_w , the natural parameter obtained post-training (related to p_w as per (2)) can vary over several orders of magnitude. To ensure numerical stability, we clip λ_w before transforming it to p_w and subsequently to z_w .

MVM operation: Consider a weight matrix \mathbf{W}^c with a corresponding parameter matrix \mathbf{Z}^c with dimensions $N \times M$. The real-valued elements of \mathbf{Z}^c is mapped to the analog conductances of the devices in WP of the crossbar with M rows and N columns. Corresponding to each column, we provision L NP cells, which are read based on a stochastic arbitration scheme to generate the required noise source. Hence, the NP portion of the crossbar is organised with L rows and N columns. The stochastic arbitration scheme is employed to reduce the effect of correlation among the weights in a column.

The MVM operation is accomplished in a row-by-row fashion. A row of WP, denoted by index j is read along with a stochastically selected row of NP, indexed by j' , to generate one row of \mathbf{W}^c , $w_j^c \in \{-1, +1\}^{N \times 1}$. Simultaneously, the j^{th} element of the input vector to the core x_j^c , is streamed into all column accumulators, to be accumulated with the sign determined by each element of w_j^c . This is repeated for each input element x_j^c by stepping through all the M rows in the WP to complete the MVM operation given in (10) and obtain output vector \mathbf{y}^c . We denote $G_{w_{j'i}^c}$ for the conductance corresponding to $w_{j'i}^c$ and $G_{n_{j'i}^c}$ for the corresponding NP cell. Mathematically, the MVM operation discussed in (10) is realised in hardware as

$$y_i^c = \sum_{j=1}^N x_j^c \times \text{sgn}(\kappa^{-1}(G_{w_{j'i}^c}^+ - G_{w_{j'i}^c}^-) + G_{n_{j'i}^c}^+ - G_{n_{j'i}^c}^-). \quad (16)$$

The stochastic arbitration is carried out by a dedicated control unit employing relatively lightweight pseudorandom generators such as linear feedback shift registers (LFSR) [42]. The sample generation and MVM operation are illustrated in Fig. 4.

C. Single Core Operations

We now discuss the details of the inference operation of a single DPCM crossbar core (Fig. 5). The size of the crossbar in the core is 144×128 , with 128 rows dedicated to WP and 16 rows dedicated to NP. Each of these areas of the crossbar have a different mechanism for row-select, therefore they each have a dedicated decoder. A DPCM cell consists of two PCM devices each with its own transistor selector arranged as a differential pair, in the standard 1T1R configuration.

Write operation: PCM devices are written or programmed through an iterative programming scheme described in [24]. This involves a program-and-verify loop where programming pulses are modulated based on the conductance read iteratively until the device reaches close to the desired conductance value. A single ADC-DAC pair is enough for this scheme – the output of the current-to-voltage converter shown in Fig. 5 can be routed to ADC input via a multiplexer (this multiplexer is different from the one shown in Fig. 5), and the DAC access can be provided via the decoders. The source line (SL) multiplexing ensures that the other devices are not switched on when a device is being programmed. The write circuitry can

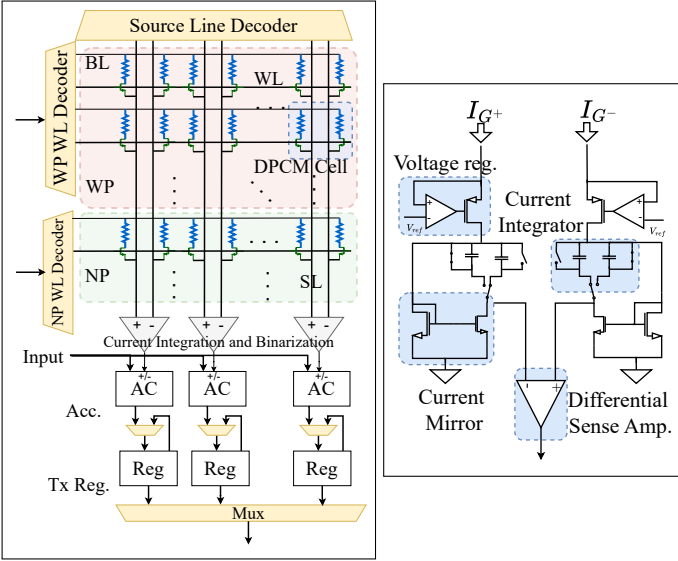


Fig. 5: **Left:** Detailed core design, expanding on Fig. 1 and 4 illustrating all the elements in the crossbar and the periphery. After accumulation, the products are transferred to the register, labeled here as ‘Reg’. This facilitates pipelining by enabling the subsequent set of matrix-vector multiplications (MVMs) to commence while the outputs from the previous MVMs are sequentially transported out of the core. **Right:** Current integration and voltage sensing circuit. Current is converted to voltage through charge integration with ping-pong mode capacitor. A current mirror-based current divider is used to reduce the integrating current to capacitor. Sense amplifier binarizes the voltage to generate the weight samples.

be power-gated during the inference operations, and will not contribute to the inference power. By provisioning only one ADC-DAC pair per core, the total area cost of incorporating the write circuitry can also be further reduced.

Input and read operation: To execute synaptic sampling, a WP and NP row are read together so that the resultant currents are summed up by Kirchoff’s law. To this end, the bit lines are first precharged and held at the read voltage of the PCM device. Then the selected WL in WP is turned on along with the world line selected from NP using stochastic arbitration. This enables the summation of the WP and NP currents on the SL, whereupon it is amplified to a rail-to-rail voltage signal. This signal is sent to the accumulator (AC) to determine the sign of x_j . In order to implement the κ scaling required for the WP and NP devices as in (16), we vary the duration of the WL selector signal, as illustrated in Fig. 6. The duration of the turn-on pulse applied to the NP row (T_{NP}) is scaled by a factor κ compared to the duration of the pulse applied to the WP row (T_{WP}). While this has an impact on the achievable throughput, using amplitude-based encoding is challenging as it requires area and power-intensive DACs [13] and also due to the non-linear relationship between read pulses and device conductivity [43].

However, to boost the achievable throughput, we evaluate operational schemes that involve turning on several NP rows in parallel. If n_r rows are turned on, the duration of the applied

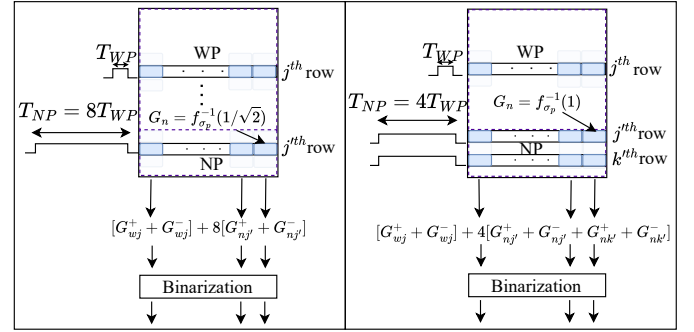


Fig. 6: Two modes of read operation – **Left:** Standard mode with $T_{NP} = 8T_{WP}$ with $n_r = 1$. **Right:** The high throughput scheme (right) that has $T_{NP} = 4T_{WP}$ with $n_r = 2$.

turn-on pulse in the NP can be reduced proportionately to T_{NP}/n_r , as long as the stored conductance values in the NP devices are also scaled appropriately as illustrated in Fig. 6. We discuss the performance with $n_r = 1$ and 2 and find that $n_r > 2$ is not feasible as the device noise available from PCM is insufficient to achieve the desired amount of noise required for synaptic sampling. The current from WP and NP is integrated as shown in Fig. 5. The current integrator, adopted from [44], consists of a current divider in the form of a mirror circuit, where the W/L ratio of the transistors involved can be adjusted to control the current ratio. This is done largely to reduce the magnitude of current integrating into the capacitor, enabling the use of smaller capacitors [13]. The differential sense amplifier then performs binarization based on the converted voltage, thereby implementing (16). As the capacitors need to be reset before being reused for integration, two capacitors in ping-pong fashion can be utilized. This way, while one capacitor discharges, the other can be employed for current integration. Upon integration, the sense amplifier, as described in [45] binarizes the converted voltage to generate $w \in \{-1, +1\}$.

MAC: During the synaptic sampling operation, the 8-bit elements of input vector x_j^c are streamed one-by-one to the corresponding 16-bit accumulators. The accumulator is responsible for summing up the individual contributions of input-weight dot product in M accumulation cycles as described in (16). This is accomplished by adding or subtracting x_j from the partial MAC value based on its sign determined by w_{ji} . This way, we avoid power- and area-hungry multi-bit ADCs. Upon accumulating the pre-neuron output for all the rows described in (16), they are then sent to the transfer registers that hold the pre-neuron outputs as they are transferred out of the core via the bus to which all the column outputs are multiplexed. Transfer registers allow the pipelining of the whole operation – while the previous pre-neuron outputs are waiting to be transferred out, the next set of MVM operations are simultaneously underway in the accumulator.

Multi-core operation: Since most typical layers in neural networks are larger than the size of a Bayes2IMC core (144×128), a layer is usually mapped across multiple cores [18]. We refer to a collection of such cores as a tile. Partial sums of such cores are then carried out across all the cores. The partial sums are then routed into a tile-level neuron

processing unit performing pre-activation accumulation, BN, ReLU, and max-pooling.

Batch normalization and ReLU: In conventional implementations, BN operations are folded into convolutional layers [46] as MVM operations are linear and BN only performs an affine transform on the products. In our case, however, as a non-linear operation (binarization) is required before MAC, it is necessary to perform a BN operation separately after the MVM operation. Having a BN unit per column was found to be costly because BN operations involve large digital multipliers. Besides, when a larger network is mapped into many cores, as is often the case, only a small number of cores perform BN operations, and the majority transfer the partially accumulated sum to the tile accumulator. Therefore we employ one BN multiplier and adder unit at each tile, significantly reducing area and power. BN coefficients can be stored in a small memory array, either built with SRAM or with PCM devices with each device storing only one-bit [47]. The latter is more area and power-efficient, and because it is stored in a binary fashion by programming the devices to $\{0, G_{max}\}$ which also ensures sufficient margin between the two levels.

Post inference processing: The entire software-trained network can be thus deployed across various such cores of the Bayes2IMC architecture. Once the results of the operations from the last layer are available, they are streamed out of the core to perform logit corrections, followed by softmax to obtain probabilities in a dedicated unit off-tile. The entire operation is repeated N_{MC} multiple times to get an ensemble of predictions (i.e. ensembling-in-time).

Frequentist networks: We note that the same core design can be easily utilized to perform frequentist inference. The weights $|w|$ can be scaled to $|G_{max}|$ before mapping. In such a case, we need not earmark parts of the crossbar for NP, and instead use all the cells to store weights $w \in \{-1, +1\}^{|w|}$, and subsequently binarize and accumulate as described above.

D. Post-Processing Logit Correction

Due to device variations, z_w will be inaccurately programmed onto the WP. Committee machines [48] have been proposed to mitigate the effects of these imperfections through ensemble averaging. However, since there is only one copy of each parameter in the ensembling-in-time paradigm adopted in this work, the programmed parameter remains unchanged across all ensembles (apart from the small effects of read noise), leaving no scope for committee-machine style parameter error smoothing. This could cause unpredictable corruption of logit distribution at the output, resulting in large variations in accuracy across multiple deployments. Therefore, we need a hardware-software co-optimized calibration operation that can be applied after mapping the network to hardware to obtain stable accuracy. We describe a logit correction scheme that is applied only on the output of the last layer during post-processing towards this.

We focus on an n -class classification problem and define the logits $l(k|\mathbf{x}, \mathbf{w}) \in \mathbb{R}$ for an input x and for each label $k \in \mathcal{C}$, such that the predicted label probability is given by the softmax of the logit vector $\mathbf{l}(\mathbf{x}, \mathbf{w}) = [l(0|\mathbf{x}, \mathbf{w}), \dots, l(n-1|\mathbf{x}, \mathbf{w})]^\top$. For any label $k \in \mathcal{C}$, the logits obtained from the available data $(\mathbf{x}, y) \sim \mathcal{D}$ under model \mathbf{w} during the

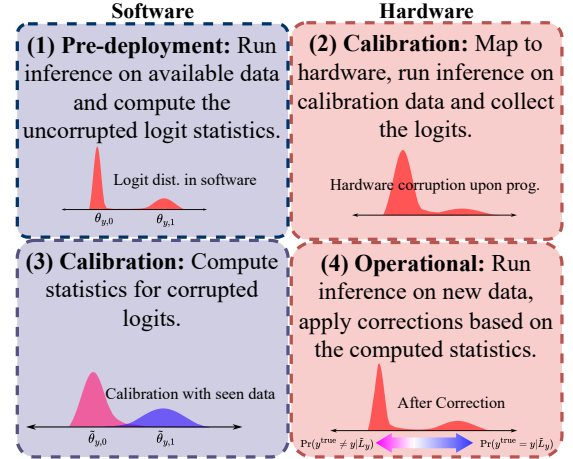


Fig. 7: A hardware-software co-optimized flow for logit correction.

pre-deployment phase are empirically observed to exhibit a bi-modal distribution consisting of two unimodal distributions $\hat{p}(L_k|y = k)$ and $\hat{p}(L_k|y \neq k)$, where $L_k = l(k|\mathbf{x}, \mathbf{w})$ is the random variable representing the empirical logit distribution on $\mathbf{x} \sim \mathcal{D}$. Both $\hat{p}(L_k|y = k)$ and $\hat{p}(L_k|y \neq k)$ are modeled as Gaussian distributions with parameters $\theta_{k,1} = (\mu_{k,1}, \sigma_{k,1})$ and $\theta_{k,0} = (\mu_{k,0}, \sigma_{k,0})$ respectively. This choice is grounded in previous works, which demonstrate that deep Bayesian neural networks converge to Gaussian processes under certain conditions [29], [49], [50], and further reinforced by empirical observations of logit distributions on our datasets.

As described before, the non-idealities of the PCM devices lead to distorted logit distributions. We denote the RV for this distribution as $\tilde{L}_k = l(k|\mathbf{x}, \tilde{\mathbf{w}})$, where $\tilde{\mathbf{w}} \in \mathcal{W}$ represents the hardware-sampled distorted model. The hardware distorted logit distribution also exhibits a bimodal structure made of distributions $\hat{p}(\tilde{L}_k|y = k)$ and $\hat{p}(\tilde{L}_k|y \neq k)$, which we model as Gaussian distributions with parameters $\hat{\theta}_{k,1} = (\tilde{\mu}_{k,1}, \tilde{\sigma}_{k,1})$ and $\hat{\theta}_{k,0} = (\tilde{\mu}_{k,0}, \tilde{\sigma}_{k,0})$, respectively.

The hardware distortions lead to reduction of resolvability of the predictions $p(y|\mathbf{w}, w)$. This results in blurring of the modes, causing degradation of separability. Since the degree of corruption cannot be predicted in advance, we developed a post-facto algorithm that corrects these distortions after the network has been mapped to hardware, illustrated in Fig. 7. During the calibration phase, we use a subset $\mathcal{D}^{cal} = \{x_i^{cal}, y_i^{cal}\}_{i=1}^{N^{cal}}$ of the available data, called calibration data, to run inference on the programmed network and estimate the Gaussian parameters $\hat{\theta}_{k,1}$ and $\hat{\theta}_{k,0}$.

We assume a one-to-one correspondence between L_y and \tilde{L}_y as an affine perturbation, such that both variables differ by scale and offset factors depending on parameters $\theta_{k,0}$, $\theta_{k,1}$, $\hat{\theta}_{k,0}$, and $\hat{\theta}_{k,1}$. If the true class y is known during the inference in operational phase, then the correction can be described as

$$\hat{l}_k = \mathbb{E}[L_k|\tilde{L}_k, y] = \frac{(\tilde{L}_k - \tilde{\mu}_{k,c})}{\tilde{\sigma}_{k,c}} \sigma_{k,c} + \mu_{k,c}, \quad (17)$$

where $c = \delta_{\{y=k\}}$. However, since the true label y is unknown at inference, we instead weight the correction by the estimated

probability of $\{y = k\}$ (depicted in Fig. 7 panel (4)) using a Bayesian update as

$$\hat{l}_k = \mathbb{E}[L_k | \tilde{L}_k] \quad (18)$$

$$\begin{aligned} &= \Pr(y = k | \tilde{L}_k) \mathbb{E}[L_k | \tilde{L}_k, y = k] \\ &\quad + \Pr(y \neq k | \tilde{L}_k) \mathbb{E}[L_k | \tilde{L}_k, y \neq k], \end{aligned} \quad (19)$$

where

$$\begin{aligned} \Pr(y = k | \tilde{L}_k) &= \frac{\Pr(y = k) \Pr(\tilde{L}_k | y = k)}{\Pr(\tilde{L}_k)} \\ &= \frac{\Pr(y = k) \mathcal{N}(\tilde{L}_k | \tilde{\mu}_{k,1}, \tilde{\sigma}_{k,1})}{\Pr(y = k) \mathcal{N}(\tilde{L}_k | \tilde{\mu}_{k,1}, \tilde{\sigma}_{k,1}) + \Pr(y \neq k) \mathcal{N}(\tilde{L}_k | \tilde{\mu}_{k,0}, \tilde{\sigma}_{k,0})} \end{aligned} \quad (20)$$

and where $\Pr(y \neq k | \tilde{L}_k)$ is computed in a similar fashion. For a balanced dataset, prior probabilities $\Pr(y = k)$ and $\Pr(y \neq k)$ are equal to $\frac{1}{n}$ and $\frac{n-1}{n}$, respectively. Accordingly, the posterior probabilities $\Pr(y = k | \tilde{L}_k)$ and $\Pr(y \neq k | \tilde{L}_k)$ determine the strength of correction application (scale and shift) towards either side, decreasing the fuzziness between the two modes. The process is repeated for each of the N_{MC} predictors in the ensemble. As these operations are performed only on the output layer, they can be handled by a dedicated computational block off-tile, amortizing the overall cost.

E. Drift compensation

In this section, we discuss techniques to compensate the effects of drift. As discussed earlier, due to structural relaxation, PCM devices exhibit a state-dependent drifting of their conductance values. The observed conductance drift has an exponential dependence on time, with the drift exponent being state-dependent [24]. Mathematically, the device conductance at time t is given as

$$G(t) = G(T_0) \left(\frac{t}{T_0} \right)^{-\nu}, \quad (21)$$

where $G(T_0)$ is the conductance at time T_0 after programming, and ν is the state dependent drift exponent. Here, $T_0 = 20$ s is the time after programming at which the noise characteristics are defined as per [24].

Two compensation mechanisms for drift compensation were suggested in [24] – Global Drift Compensation (GDC) and Adaptive Batch Normalization Scheme (AdaBS). These methods require periodic calibration applied to each layer of the network with a subset of the known data. In the former, the MVM output of a column is measured at various time instances and divided with the outputs obtained immediately after the instantiation of the array, to gauge the extent of compensation required. The compensation factor thus calculated is used to scale the measured MVM products to reverse the effect due to drift. The latter uses running batch statistics instead of MVM outputs to calculate the compensations per layer. Both these methods measure the MVM output to estimate the extent of drift. This is necessary as individual weights drift at state-dependent rates, making a uniform, one-size-fits-all compensation impossible.

We describe how the reparametrization techniques introduced in this paper enable a straightforward and universal

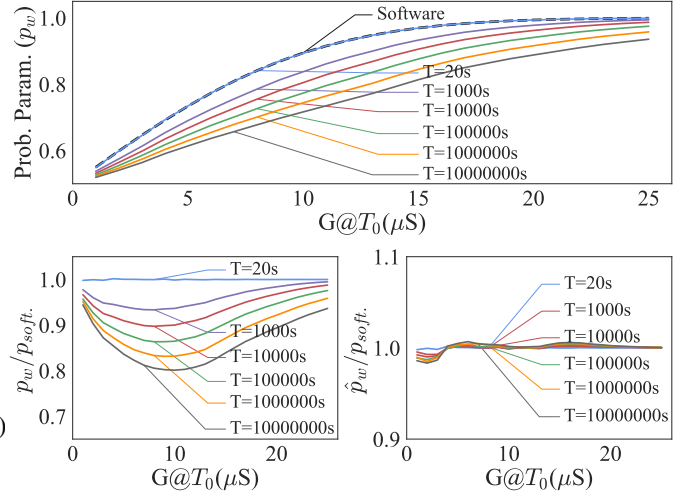


Fig. 8: **Top:** p_w , the probability parameter for a weight w vs WP conductance G at $T_0 = 20$ s. **Bottom, Left:** Ratio of p_w and $p_{soft.}$, the ideal, software calculated value of p_w . **Bottom, Right:** Ratio of p_w by $p_{soft.}$ after applying correction α_t .

drift compensation method applicable to all the layers of any BBNN that does not have these limitations. Our approach, Bayes2IMC drift compensation (BBDC), involves using a single drift correction coefficient $\alpha_t = \left(\frac{t}{T_0}\right)^{\nu_c}$ to scale the duration of the read pulses applied to measure the device conductances to reverse drift effects.

To select the appropriate value of ν_c , we examine how drift affects p_w . Since the reparametrized probability parameter z_w is directly proportional to the conductance state, it is significantly influenced by drift. However, the impact of drift on p_w is much less pronounced, as illustrated in Fig. 8. We observe that conductance values near the extremes of our range (0 and $25\mu\text{S}$) are less affected by drift. Therefore, we select $\nu_c = 0.06$, corresponding to the drift exponent at approximately $G = 8\mu\text{S}$, and apply this correction across the entire network. This choice effectively minimizes errors in p_w within the mid-conductance ranges while causing minimal changes at the extremes. As a result, the reparametrization of p_w into z_w enables a straightforward drift compensation across the entire conductance range. The effect of compensating factor α_t is illustrated in Fig. 8, which shows the relationship between $p_{soft.}$, the software calculated ideal probability parameters, p_w , and \hat{p}_w , the probability parameter after compensation.

The effect of drift on noise sourced from NP was empirically observed to be smaller than the magnitude of WP conductance. Therefore, we perform drift compensation by appropriately adjusting T_{NP} to adjust the relative durations of the read pulses applied to WP and NP. Since T_{NP} can only be integral multiples of T_{WP} , our scaling is quantized. We show in section IV-C that this quantization has no impact on accuracy performance, and we can effectively correct for the accuracy degradation caused by drift. We also note that T_{NP} reduces with time. As the throughput of the Bayes2IMC core depends on T_{NP} since each parameter read operation needs that long to complete, we achieve a throughput speedup with time. This, however, comes at the cost of overall inference

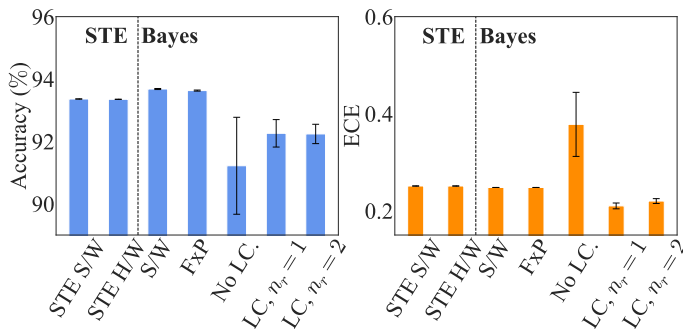


Fig. 9: Accuracy and ECE on CIFAR-10. The first two bars on the left of the dashed line correspond to the frequentist-STE based network while the rest correspond to the BBNN. LC refers to the logit correction. The error bars indicate ± 1 standard deviation (SD).

power consumption, as discussed in section IV.

Thus, by calculating a single multiplying factor, α_t , at time t based on the drift behavior of PCM devices and then adjusting the read pulses, we can effectively mitigate the effects of drift. Our approach is robust and does not require calibration with known data to correct drift degradation, making it more versatile. However, the logit correction described in sec. III-D may still require such calibration. When combined with drift compensation, logit correction can further enhance accuracy and ECE stability.

IV. EXPERIMENTS AND RESULTS

In this section, we evaluate the performance of the proposed Bayes2IMC architecture. We first train a VGGBinaryConnect network on CIFAR-10 dataset. VGGBinaryConnect is a modified version of a 9-layer frequentist VGG network with binary synapses described in [51] and [52]. Its BBNN counterpart was trained using the BayesBiNN optimizer described in [34]. For benchmarking, the frequentist version of the same network was trained using a Straight-Through Estimator (STE) with ADAM optimizer, as described in [34]. The BBNN network was then transferred to a custom PCM hardware simulator implementing the noise characteristics described in Fig. 3 as well as appropriate input and accumulator quantization. Inference was then performed with $N_{MC} = 10$. The logit correction method discussed in sec. III-D were calibrated with 2000 validation set images. All the results were reported from 6 different runs for each scenario, with each run comprising of (in case of a hardware implementation) an initial device programming step followed by inference. Accuracy, ECE, and uncertainty quantification results were obtained under various scenarios. Drift performance was evaluated for up to $T = 10^7$ s. Finally, hardware projections were calculated for the Bayes2IMC architecture and compared with equivalent SRAM architecture and existing implementations in the literature.

A. Accuracy and ECE Performance

Accuracy and ECE evaluated on hardware (with logits corrected and uncorrected) were benchmarked against FP32 software network, a frequentist STE-based network, and a fixed point (FxP) implementation (Fig. 9). The fixed point network

was parametrized with 5-bit parameters for a fair comparison with a PCM implementation, as the effective PCM bit capacity is reported to be 4 [53] making DPCM capacity 5-bits. The frequentist network was also transferred to PCM simulator for hardware simulation.

The software classification accuracy of BBNN (93.68% for FP32 and 93.63% for fixed-point) is slightly better compared to the STE-based frequentist network (93.36%). This matches the accuracy reported in literature [34]. The estimated ECE values for both are found to be comparable.

There is no drop in accuracy or ECE for the frequentist STE network post-transfer to hardware. This is expected because devices are mapped to only two conductance levels. In contrast, the uncorrected Bayes2IMC accuracy post-mapping are poorer (91.22%) with high cross-deployment variations ($\sim \pm 1.5\%$). Upon applying corrections to the logits, the accuracy variations were brought down to 0.4%. The correction boosts accuracy while decreasing ECE as well, with accuracy reaching within 1.5% of the ideal software accuracy (92.26% vs 93.68%) and ECE slightly improving in comparison to the FP32 software implementation (0.21 vs 0.25).

We also compare the performance of the two read schemes introduced in section III-C; for both $n_r = 2$ and $n_r = 1$ we obtain similar accuracy and ECE. This validates the multiple NP row read method introduced to increase throughput.

B. Uncertainty Quantification

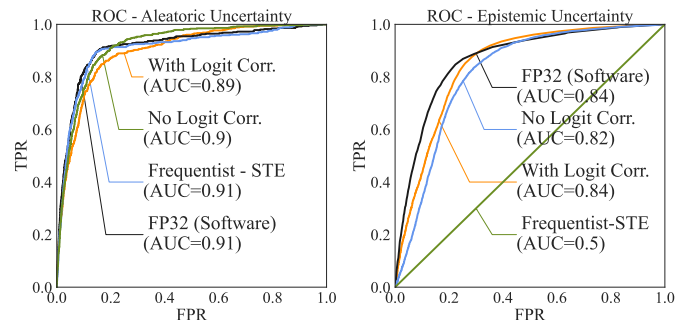


Fig. 10: ROC of U_a (Left) and U_e (Right), for FP32 (software), frequentist, uncorrected and corrected logit scenarios (hardware).

Uncertainty is quantified by entropy measures as described in (6), (7) and (8). For each input data, the aleatoric (U_a) and epistemic uncertainties (U_e) are computed. Aleatoric uncertainty (U_a) helps determine whether the prediction is correct or incorrect, while epistemic uncertainty (U_e) identifies whether the input is IND or OOD, based on predefined thresholds. To evaluate the ability of the network to discriminate across all thresholds, we plot receiver operating characteristic (ROC) curves. For aleatoric uncertainty, the ROC curve measures the ability to differentiate between correct and incorrect predictions. For epistemic uncertainty, the ROC curve evaluates the ability to distinguish between IND and OOD data, with the CIFAR100 dataset used for OOD detection [10]. The area under the curve (AUC) of each ROC is used as the metric to evaluate the uncertainty quantification performance.

We compared the performance of Bayes2IMC with uncorrected as well as corrected logits against software networks

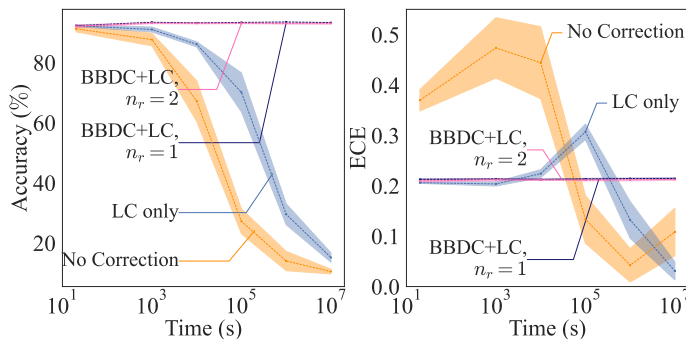


Fig. 11: Effect of drift on accuracy and ECE performance. The band around lines represent ± 1 SD.

(Fig. 10). The AUC for both epistemic and aleatoric uncertainties for Bayes2IMC, with and without logit correction are found to be closely matching the FP32 software network AUC. The aleatoric uncertainty of the Bayes2IMC matches that of the frequentist-STE network, while the epistemic uncertainty AUC for the frequentist counterpart is 0.5. This is because $U_e = 0$ for all inputs for a frequentist network, indicating its inability to discriminate between OOD and IND data.

C. Drift Mitigation

The effect of drift on accuracy and ECE was studied up to $T = 10^7$ s, as shown in Fig. 11. We observe that accuracy as well as ECE degrades significantly due to conductance drift. With no correction, the net accuracy of the network comes down nearly to 10% in 10^6 s, which is equivalent to random guessing. In around 10^5 s, i.e., slightly longer than a day, the accuracy reduces to 20%. Logit correction slightly improve the performance – with accuracy post correction at 10^5 s being around 70%. It is worth noting that it takes around 10^6 s for the accuracy of the output of Bayes2IMC to reduce to 10% without any corrections. This is significantly longer than the time taken by analog PCM implementations such as [47], where the time taken for the accuracy to reduce to random guessing without any drift mitigation strategy is around 1000 s. The reparametrization of p_w to z_w before mapping, rather than mapping p_w directly, ensured significant robustness to drift, as seen in Fig. 8.

The sharp drop of ECE from 10^5 s onwards is accompanied by a severe decline in accuracy around the same time in both uncorrected and logit-corrected scenarios. This does not imply ECE performance improvement, because ECE only quantifies the divergence between accuracy and prediction confidence. Therefore, it is important to look at ECE in the context of the accuracy performance and not as a standalone metric.

Upon applying BBDC technique introduced in this paper, we achieve a complete recovery of accuracy performance through 10^7 s. We also compare the uncertainty estimation performance of various correction methods in conjunction with BBDC. This is accomplished by plotting AUC of ROCs for epistemic and aleatoric uncertainty across all time instances, as shown in Fig. 12. Without BBDC, the AUC for both U_e and U_a suffers significant performance degradation, collapsing to near 0.5. With BBDC, the aleatoric and epistemic uncertainty performance completely recovers, and the results from both

	Units	PCM	SRAM
Clock Rate	MHz	100	208
Ops/clock pulse (8/4/2)	-	16/32/64	128
Read power per weight	μ W	48.5	1993
Total read power	mW	6.2	256
Total digital block power (8/4/2)	mW	1.46/2.92/5.84	26.6
Total power (8/4/2)	mW	7.6/9.1/12.0	282
Total core area	mm ²	0.015	0.14
Total sensing block area	mm ²	0.02	0.04
Total digital block area	mm ²	0.18	0.2
Total BN memory area	mm ²	0.002	0.007
Total area	mm ²	0.22	0.40
Power efficiency (8/4/2)	GOPS/W	208/350/531	94.6
Total efficiency (8/4/2)	GOPS/W/mm ²	941/1581/2397	250

corrected and uncorrected logits closely match.

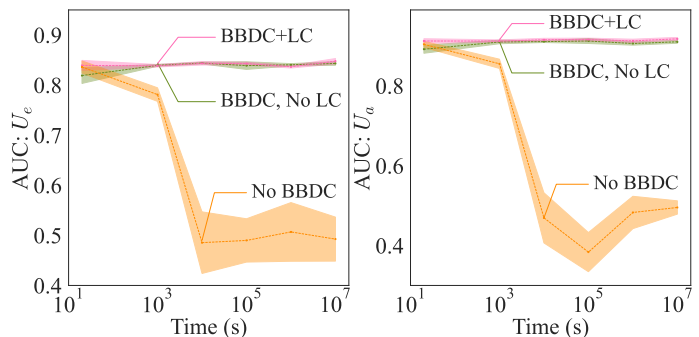


Fig. 12: Epistemic and aleatoric uncertainty due to effect of conductance drift under following scenarios: no drift compensation, drift compensation with logits uncorrected, and drift compensation with logit correction.

D. Hardware Estimation

We now estimate the hardware performance of the Bayes2IMC architecture in terms of throughput, area, and power of a single Bayes2IMC PCM core and compare it with an equivalent SRAM core with 5-bit parameters.

Our simulations are based on large-array PCM hardware results reported in the literature by IBM Research where the memristive device was integrated with industry-standard 90 nm CMOS technology. Hence, we consider 90 nm node for our hardware projections incorporating the device noise characteristics based on PCM cells fabricated in this node [24]. The cell read power and area for PCM devices used here are based on [45]. SRAM read power is assumed to follow the trends reported in [54], [55], and scaled to equivalent numbers

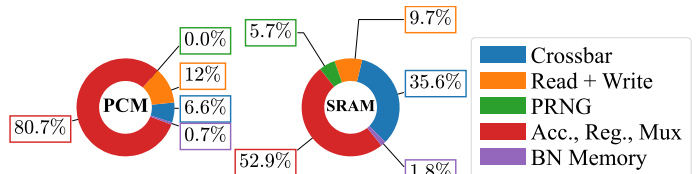


Fig. 13: Area breakdown of a PCM and an SRAM core.

TABLE III: Comparison with other works in literature

	Units	[57]	[58]	[21]	[59]	[9]	This work
Network	-	MLP	ResNet-18	MLP	MLP	VGG-16	VGGBinaryConnect
Dataset	-	MNIST	CIFAR-10	MNIST	MNIST	CIFAR-10	CIFAR-10
Parameter distribution	-	Gaussian	Gaussian	Gaussian	Gaussian	Gaussian	Binary
Weight precision	bits	8	8	8	8	8	1
Accuracy on CIFAR-10	%	-	92.9	-	-	88	92.2
Implementation	-	FPGA	FPGA	DW-MTJ	CMOS ASIC	SOT-MRAM	PCM
Node	nm	28	20	28	45	22	90
Throughput	GOPS	59.6	1590	-	1.86	92	6.4
Area	mm ²	-	-	-	6.63	-	0.22
Power	W	6.11	45	-	0.5	0.0089	0.012
Power efficiency	GOPS/W	9.75	35.33	2516	3.72	10387	531
Total efficiency	GOPS/W/mm ²	-	-	-	0.5611	-	2568
Power efficiency (90nm)	GOPS/W	0.42	0.91	175.82	0.86	447.3	531
Total efficiency (90nm)	GOPS/W/mm ²	-	-	-	0.046	-	2568

for the 90 nm node using scaling laws described in [56]. Cell area of a single PCM was taken to be $29F^2$ per device as per [45], whereas that of a 6T SRAM-based cell was taken to be $120F^2$ [18]. We consider a 128×128 parameter storage per crossbar for both PCM and SRAM core. Additionally, 16 rows are apportioned for NP, taking the total number of PCM core rows to 144. While each row read in SRAM requires only a single clock cycle, the PCM architecture requires 8 clock pulses for $n_r = 1$ and 4 clock pulses for $n_r = 2$, as per Fig. 6. For the $n_r = 2$ scenario, the read pulse width can shrink to 2 clock pulses at around 10^7 s because of drift compensation.

The digital peripheral circuits, including accumulators, registers and multiplexers were synthesized in Cadence. The operating frequency for Bayes2IMC is assumed to be 100 MHz, based on the read pulse time required for the PCM device read as per [45]. Since the total read time is determined by T_{NP} , the digital peripheral circuit is clocked at the same rate to synchronize operations. Thus, the speed-up of the core comes at the cost of read power. For an SRAM core, the frequency was calculated based on the timing report obtained from Cadence synthesis.

Fig. 13 shows the area breakdown of an PCM Bayes2IMC and the SRAM core respectively. In a Bayes2IMC PCM core, the digital peripheral circuitry—consisting of the accumulator, register, multiplexer block, and decoders—accounts for the majority of the overall area, making up 82% of the footprint. In contrast, for SRAM, the crossbar area is comparable to the size of the peripheral area. Because of the dominance of peripherals, the total area of PCM core is only $2\times$ smaller than that of SRAM even though the PCM crossbar is almost $14\times$ smaller than its SRAM counterpart.

The digital peripheral circuitry in latter also consists of the PRNG unit, which was designed with maximal reuse architecture discussed in [8], where all 4-bytes on a 32 bit LFSR were utilized for random number generation. The PRNG unit makes up almost 10% of total peripheral area and 6% of the total core area. Additionally, we highlight the area required to store 128 pairs of BN coefficients, one per column.

Table II also compares the power consumed by the SRAM and the Bayes2IMC core. Owing to the increase in clock rates due to the decrease in T_{NP} , we have reported the power for three modes, indicated as 8/4/2 corresponding to $n_r = 1$,

$n_r = 2$, and for $T_{NP}/T_{WP} = 2$ at $t = 10^7$ for $n_r = 2$ respectively.

We evaluate efficiency for the three modes of operation (with read pulses 8/4/2 indicated in Table II) as discussed earlier. We find that the PCM core architecture has power efficiency (in Giga-operations per second per Watt or GOPS/W) of $2.2\times$ for $T_{NP}/T_{WP} = 8$, $3.7\times$ for $T_{NP}/T_{WP} = 4$ and $5.6\times$ for $T_{NP}/T_{WP} = 2$ mode, compared to an SRAM core. Overall efficiency (GOPS/W/mm²) gains are respectively $3.8\times$, $6.3\times$, and $9.6\times$.

We also compare our work with other works on Bayesian neural network architectures reported in literature. These include implementations on CMOS (FPGA and ASIC), as well as on NVM devices such as DW-MTJ and SOT-MRAM utilizing nanoscale stochasticity. We compute the power efficiency in terms of GOPS/W and total efficiency in terms of GOPS/W/mm². For fair comparison, we translate these numbers to 90 nm node equivalent using scaling laws described in [56]. We find that our design achieves one of the best accuracies on CIFAR-10 despite having single-bit weights. It also outperforms all CMOS architectures as well as the DW-MTJ (iso-node) implementation in terms of area and power efficiency. We also have $1.2\times$ better best-case ($T_{NP}/T_{WP} = 2$) and comparable nominal case ($0.78\times$ @ $T_{NP}/T_{WP} = 4$) iso-node power efficiency compared to the recent state-of-the-art [9]. Note that the approach reported in [9] achieves high efficiency by performing ensembling only on selected layers, as well as by utilizing selector-less, high-speed, SOT-MRAM cells.

V. CONCLUSION

This work introduced Bayes2IMC, a binary Bayesian neural network implemented with in-memory computing on standard PCM crossbar hardware. By leveraging the conductance variations of PCM devices—typically considered a drawback—for ensembling, we reduced the core peripheral area by nearly 10% compared to an SRAM based core that utilizes a digital pseudo-random number generator. Our approach includes a reparametrization algorithm and an innovative scheme that eliminates the need for ADCs, significantly enhancing both power and area efficiency.

Through a hardware-software co-optimization flow, output logits were corrected to enhance accuracy and the expected

calibration error. Additionally, the reparametrization technique supports a straightforward drift compensation method that fully mitigates drift-induced accuracy degradation. We also successfully demonstrated uncertainty quantification and decomposition into aleatoric and epistemic uncertainties using Bayes2IMC.

Our hardware projections, informed by literature and CAD projections, indicate that while Bayes2IMC operates $2 - 8\times$ slower than an SRAM-based architecture, it achieves up to $10\times$ higher efficiency in terms of GOPS/W/mm². We also projected that Bayes2IMC is up to 20% more power-efficient compared to the state-of-the-art. Our analysis reveals that the peripheral circuitry, both digital and analog, contributes significantly more to area and power consumption than the crossbar or memory elements themselves. Future efforts to improve efficiency must thus focus on optimizing peripheral circuits.

The techniques, algorithms, and co-optimization framework discussed in this paper are demonstrated with PCM devices but are versatile enough to be applied to other noisy NVM device-based compute architectures for implementing binary Bayesian networks.

ACKNOWLEDGMENT

BR's research was supported in part by the EPSRC Open Fellowship EP/X011356/1 and by the EPSRC grant EP/X011852/1. OS's research was supported by an Open Fellowship of the EPSRC with reference EP/W024101/1, by the EPSRC project EP/X011852/1, and by the European Union's Horizon Europe Project CENTRIC under Grant 101096379.

REFERENCES

- [1] N. Band, T. G. J. Rudner, Q. Feng, A. Filos, Z. Nado, M. Dusenberry, G. Jerfel, D. Tran, and Y. Gal, "Benchmarking Bayesian deep learning on diabetic retinopathy detection tasks," in *Proceedings of the Neural Information Processing Systems Track on Datasets and Benchmarks*, J. Vanschoren and S. Yeung, Eds., vol. 1, 2021.
- [2] A. Kendall and Y. Gal, "What Uncertainties Do We Need in Bayesian Deep Learning for Computer Vision?" in *Proceedings of the 31st International Conference on Neural Information Processing Systems*, ser. NIPS'17. Red Hook, NY, USA: Curran Associates Inc., 2017, p. 5580–5590.
- [3] F. Tambon, G. Laberge, L. An, A. Nikanjam, P. S. N. Mindom, Y. Pequignot, F. Khomh, G. Antoniol, E. Merlo, and F. Laviolette, "How to certify machine learning based safety-critical systems? A systematic literature review," *Automated Software Engineering*, vol. 29, no. 2, p. 38, 2022.
- [4] C. Guo, G. Pleiss, Y. Sun, and K. Q. Weinberger, "On calibration of modern neural networks," in *International Conference on Machine Learning*. PMLR, 2017, pp. 1321–1330.
- [5] J. Huang, S. Park, and O. Simeone, "Calibrating Bayesian learning via regularization, confidence minimization, and selective inference," *arXiv preprint arXiv:2404.11350*, 2024.
- [6] P. Katti, N. Skatchkovsky, O. Simeone, B. Rajendran, and B. M. Al-Hashimi, "Bayesian Inference on Binary Spiking Networks Leveraging Nanoscale Device Stochasticity," in *2023 IEEE International Symposium on Circuits and Systems (ISCAS)*, 2023, pp. 1–5.
- [7] H. Jang, N. Skatchkovsky, and O. Simeone, "BiSNN: Training spiking neural networks with binary weights via Bayesian learning," in *2021 IEEE Data Science and Learning Workshop (DSLW)*. IEEE, 2021.
- [8] P. Katti, A. Nimbekar, C. Li, A. Acharyya, B. M. Al-Hashimi, and B. Rajendran, "Bayesian Inference Accelerator for Spiking Neural Networks," in *2024 IEEE International Symposium on Circuits and Systems (ISCAS)*, 2024.
- [9] A. Lu, Y. Luo, and S. Yu, "An algorithm-hardware co-design for Bayesian neural network utilizing SOT-MRAM's inherent stochasticity," *IEEE Journal on Exploratory Solid-State Computational Devices and Circuits*, vol. 8, no. 1, pp. 27–34, 2022.
- [10] D. Bonnet, T. Hirtzlin, A. Majumdar, T. Dalgaty, E. Esmanhotto, V. Meli, N. Castellani, S. Martin, J.-F. Nodin, G. Bourgeois *et al.*, "Bringing uncertainty quantification to the extreme-edge with memristor-based Bayesian neural networks," *Nature Communications*, vol. 14, no. 1, p. 7530, 2023.
- [11] W. A. Wulf and S. A. McKee, "Hitting the memory wall: Implications of the obvious," *ACM SIGARCH computer architecture news*, vol. 23, no. 1, pp. 20–24, 1995.
- [12] S. Jain, A. Ankit, I. Chakraborty, T. Gokmen, M. Rasch, W. Haensch, K. Roy, and A. Raghunathan, "Neural network accelerator design with resistive crossbars: Opportunities and challenges," *IBM Journal of Research and Development*, vol. 63, no. 6, pp. 10–1, 2019.
- [13] F. Aguirre, A. Sebastian, M. Le Gallo, W. Song, T. Wang, J. J. Yang, W. Lu, M.-F. Chang, D. Ielmini, Y. Yang *et al.*, "Hardware implementation of memristor-based artificial neural networks," *Nature Communications*, vol. 15, no. 1, p. 1974, 2024.
- [14] G. Verma, A. Nisar, S. Dhull, and B. K. Kaushik, "Neuromorphic accelerator for spiking neural network using SOT-MRAM crossbar array," *IEEE Transactions on Electron Devices*, 2023.
- [15] C.-J. Jhang, C.-X. Xue, J.-M. Hung, F.-C. Chang, and M.-F. Chang, "Challenges and trends of SRAM-based computing-in-memory for AI edge devices," *IEEE Transactions on Circuits and Systems I: Regular Papers*, vol. 68, no. 5, pp. 1773–1786, 2021.
- [16] A. Agrawal, A. Jaiswal, C. Lee, and K. Roy, "X-SRAM: Enabling In-Memory Boolean Computations in CMOS Static Random Access Memories," *IEEE Transactions on Circuits and Systems I: Regular Papers*, vol. 65, no. 12, pp. 4219–4232, 2018.
- [17] S. Mittal, G. Verma, B. Kaushik, and F. A. Khanday, "A survey of SRAM-based in-memory computing techniques and applications," *Journal of Systems Architecture*, vol. 119, p. 102276, 2021.
- [18] X. Peng, S. Huang, Y. Luo, X. Sun, and S. Yu, "DNN+ NeuroSim: An end-to-end benchmarking framework for compute-in-memory accelerators with versatile device technologies," in *2019 IEEE International Electron Devices Meeting (IEDM)*. IEEE, 2019, pp. 32.5.1–32.5.4.
- [19] A. Kneip and D. Bol, "Impact of analog non-idealities on the design space of 6T-SRAM current-domain dot-product operators for in-memory computing," *IEEE Transactions on Circuits and Systems I: Regular Papers*, vol. 68, no. 5, pp. 1931–1944, 2021.
- [20] Y. Ma, Y. Qiu, W. Zhao, G. Li, M. Wu, T. Jia, L. Ye, and R. Huang, "DCIM-GCN: Digital Computing-in-Memory Accelerator for Graph Convolutional Network," *IEEE Transactions on Circuits and Systems I: Regular Papers*, 2024.
- [21] K. Yang, A. Malhotra, S. Lu, and A. Sengupta, "All-spin Bayesian neural networks," *IEEE Transactions on Electron Devices*, vol. 67, no. 3, pp. 1340–1347, 2020.
- [22] S. Yu, W. Shim, X. Peng, and Y. Luo, "RRAM for compute-in-memory: From inference to training," *IEEE Transactions on Circuits and Systems I: Regular Papers*, vol. 68, no. 7, pp. 2753–2765, 2021.
- [23] R. Khaddam-Aljameh, M. Stanisavljevic, J. F. Mas, G. Karunaratne, M. Braendli, F. Liu, A. Singh, S. M. Müller, U. Egger, Petropoulos *et al.*, "HERMES core—a 14nm CMOS and pcm-based in-memory compute core using an array of 300ps/LSB linearized CCO-based ADCs and local digital processing," in *2021 Symposium on VLSI Circuits*. IEEE, 2021.
- [24] V. Joshi, M. Le Gallo, S. Haefeli, I. Boybat, S. R. Nandakumar, C. Piveteau, M. Dazzi, B. Rajendran, A. Sebastian, and E. Eleftheriou, "Accurate deep neural network inference using computational phase-change memory," *Nature Communications*, vol. 11, no. 1, pp. 1–13, 2020.
- [25] P.-Y. Chen, D. Kadetotad, Z. Xu, A. Mohanty, B. Lin, J. Ye, S. Vrudhula, J.-s. Seo, Y. Cao, and S. Yu, "Technology-design co-optimization of resistive cross-point array for accelerating learning algorithms on chip," in *2015 Design, Automation & Test in Europe Conference & Exhibition (DATE)*. IEEE, 2015, pp. 854–859.
- [26] T. Dalgaty, N. Castellani, C. Turck, K.-E. Harabi, D. Querlioz, and E. Vianello, "In situ learning using intrinsic memristor variability via Markov chain Monte Carlo sampling," *Nature Electronics*, vol. 4, no. 2, pp. 151–161, 2021.
- [27] T. Salimans, D. Kingma, and M. Welling, "Markov chain monte carlo and variational inference: Bridging the gap," in *International Conference on Machine Learning*. PMLR, 2015, pp. 1218–1226.
- [28] S. T. Ahmed, K. Danouchi, C. Münch, G. Prenat, L. Anghel, and M. B. Tahoori, "Spindrop: Dropout-based Bayesian binary neural networks

- with spintronic implementation,” *IEEE Journal on Emerging and Selected Topics in Circuits and Systems*, vol. 13, no. 1, pp. 150–164, 2023.
- [29] Y. Gal and Z. Ghahramani, “Dropout as a Bayesian Approximation: Representing Model Uncertainty in Deep Learning,” in *Proceedings of The 33rd International Conference on Machine Learning*, ser. Proceedings of Machine Learning Research, M. F. Balcan and K. Q. Weinberger, Eds., vol. 48. New York, New York, USA: PMLR, 20–22 Jun 2016, pp. 1050–1059.
- [30] L. V. Jospin, H. Laga, F. Boussaid, W. Buntine, and M. Bennamoun, “Hands-On Bayesian Neural Networks—A Tutorial for Deep Learning Users,” *IEEE Computational Intelligence Magazine*, vol. 17, no. 2, pp. 29–48, 2022.
- [31] A. Chan, A. Alaa, Z. Qian, and M. Van Der Schaar, “Unlabelled data improves Bayesian uncertainty calibration under covariate shift,” in *Proceedings of the 37th International Conference on Machine Learning*, ser. Proceedings of Machine Learning Research, H. D. III and A. Singh, Eds., vol. 119. PMLR, 13–18 Jul 2020, pp. 1392–1402.
- [32] A. G. Wilson, “The case for Bayesian deep learning,” *arXiv preprint arXiv:2001.10995*, 2020.
- [33] M. E. Khan and H. Rue, “The Bayesian learning rule,” *Journal of Machine Learning Research*, vol. 24, no. 281, pp. 1–46, 2023.
- [34] X. Meng, R. Bachmann, and M. E. Khan, “Training binary neural networks using the Bayesian learning rule,” in *International Conference on Machine Learning*. PMLR, 2020, pp. 6852–6861.
- [35] O. Simeone, *Machine Learning for Engineers*, 1st ed. Cambridge University Press, Nov. 2022. [Online]. Available: <https://www.cambridge.org/highereducation/product/9781009072205/book>
- [36] S. R. Nandakumar, M. Le Gallo, I. Boybat, B. Rajendran, A. Sebastian, and E. Eleftheriou, “A phase-change memory model for neuromorphic computing,” *Journal of Applied Physics*, vol. 124, no. 15, p. 152135, 2018. [Online]. Available: <https://doi.org/10.1063/1.5042408>
- [37] B. Rajendran, A. Sebastian, and E. Eleftheriou, “Building next-generation AI systems: Co-optimization of algorithms, architectures, and nanoscale memristive devices,” in *2019 IEEE 11th International Memory Workshop (IMW)*. IEEE, 2019, pp. 1–4.
- [38] N. Papandreou, H. Pozidis, A. Pantazi, A. Sebastian, M. Breitwisch, C. Lam, and E. Eleftheriou, “Programming algorithms for multilevel phase-change memory,” in *2011 IEEE International Symposium of Circuits and Systems (ISCAS)*. IEEE, 2011, pp. 329–332.
- [39] M. Le Gallo and A. Sebastian, “Chapter 3 - Phase-change memory,” in *Memristive Devices for Brain-Inspired Computing*, ser. Woodhead Publishing Series in Electronic and Optical Materials, S. Spiga, A. Sebastian, D. Querlioz, and B. Rajendran, Eds. Woodhead Publishing, 2020, pp. 63–96.
- [40] M. Gibbs, J. Evetts, and J. Leake, “Activation energy spectra and relaxation in amorphous materials,” *Journal of Materials Science*, vol. 18, pp. 278–288, 1983.
- [41] E. Jang, S. Gu, and B. Poole, “Categorical Reparameterization with Gumbel-Softmax,” in *International Conference on Learning Representations*, 2017.
- [42] K. K. Saluja, “Linear feedback shift registers theory and applications,” *Department of Electrical and Computer Engineering, University of Wisconsin-Madison*, pp. 4–14, 1987.
- [43] P.-Y. Chen, D. Kadetotad, Z. Xu, A. Mohanty, B. Lin, J. Ye, S. Vrudhula, J.-s. Seo, Y. Cao, and S. Yu, “Technology-design co-optimization of resistive cross-point array for accelerating learning algorithms on chip,” in *2015 Design, Automation & Test in Europe Conference & Exhibition (DATE)*, 2015, pp. 854–859.
- [44] F. Cai, J. M. Correll, S. H. Lee, Y. Lim, V. Bothra, Z. Zhang, M. P. Flynn, and W. D. Lu, “A fully integrated reprogrammable memristor-CMOS system for efficient multiply-accumulate operations,” *Nature Electronics*, vol. 2, no. 7, pp. 290–299, 2019.
- [45] S. R. Kulkarni, S. Yin, J.-s. Seo, and B. Rajendran, “An On-Chip Learning Accelerator for Spiking Neural Networks using STT-RAM Crossbar Arrays,” in *2020 Design, Automation & Test in Europe Conference & Exhibition (DATE)*, 2020, pp. 1019–1024.
- [46] I. Pérez and M. Figueroa, “A heterogeneous hardware accelerator for image classification in embedded systems,” *Sensors*, vol. 21, no. 8, p. 2637, 2021.
- [47] V. Joshi, W. He, J.-s. Seo, and B. Rajendran, “Hybrid in-memory computing architecture for the training of deep neural networks,” in *2021 IEEE International Symposium on Circuits and Systems (ISCAS)*, 2021, pp. 1–5.
- [48] D. Joksas, P. Freitas, Z. Chai, W. H. Ng, M. Buckwell, C. Li, W. Zhang, Q. Xia, A. Kenyon, and A. Mehonic, “Committee machines—A universal method to deal with non-idealities in memristor-based neural networks,” *Nature Communications*, vol. 11, no. 1, pp. 1–10, 2020.
- [49] C. Williams, “Computing with infinite networks,” *Advances in neural information processing systems*, vol. 9, 1996.
- [50] D. Agrawal, T. Papamarkou, and J. Hinkle, “Wide neural networks with bottlenecks are deep Gaussian processes,” *Journal of Machine Learning Research*, vol. 21, no. 175, pp. 1–66, 2020.
- [51] M. Alizadeh, J. Fernández-Marqués, N. D. Lane, and Y. Gal, “An Empirical study of Binary Neural Networks’ Optimisation,” in *International Conference on Learning Representations*, 2018.
- [52] M. Courbariaux, Y. Bengio, and J.-P. David, “BinaryConnect: Training Deep Neural Networks with Binary Weights during Propagations,” in *Proceedings of the 28th International Conference on Neural Information Processing Systems - Volume 2*, ser. NIPS’15. Cambridge, MA, USA: MIT Press, 2015, p. 3123–3131.
- [53] H.-S. P. Wong, S. Raoux, S. Kim, J. Liang, J. P. Reifenberg, B. Rajendran, M. Asheghi, and K. E. Goodson, “Phase change memory,” *Proceedings of the IEEE*, vol. 98, no. 12, pp. 2201–2227, 2010.
- [54] A. Pedram, S. Richardson, M. Horowitz, S. Galal, and S. Kvatinsky, “Dark memory and accelerator-rich system optimization in the dark silicon era,” *IEEE Design & Test*, vol. 34, no. 2, pp. 39–50, 2016.
- [55] G. Datta, S. Kundu, A. R. Jaiswal, and P. A. Beerel, “ACE-SNN: Algorithm-hardware co-design of energy-efficient & low-latency deep spiking neural networks for 3D image recognition,” *Frontiers in neuroscience*, vol. 16, p. 815258, 2022.
- [56] A. Stillmaker and B. Baas, “Scaling equations for the accurate prediction of CMOS device performance from 180 nm to 7 nm,” *Integration*, vol. 58, pp. 74–81, 2017.
- [57] R. Cai, A. Ren, N. Liu, C. Ding, L. Wang, X. Qian, M. Pedram, and Y. Wang, “VIBNN: Hardware acceleration of Bayesian neural networks,” *ACM SIGPLAN Notices*, vol. 53, no. 2, pp. 476–488, 2018.
- [58] H. Fan, M. Ferienc, M. Rodrigues, H. Zhou, X. Niu, and W. Luk, “High-Performance FPGA-Based Accelerator for Bayesian Neural Networks.” IEEE Press, 2021, p. 1063–1068.
- [59] X. Jia, J. Yang, R. Liu, X. Wang, S. D. Cotofana, and W. Zhao, “Efficient Computation Reduction in Bayesian Neural Networks Through Feature Decomposition and Memorization,” *IEEE Transactions on Neural Networks and Learning Systems*, vol. 32, pp. 1703–1712, 2020.